

Unsteady Numerical Simulation of Flow around 2-D Circular Cylinder for High Reynolds Numbers

Yanhui Ai^{1,2}, Dakui Feng^{1*}, Hengkui Ye¹ and Lin Li¹

1. School of Naval Architecture and Ocean Engineering Huazhong University of Science and Technology, Wuhan 430074, China

2. 710 Institute of China Ship Heavy Industry Group Corporation, Yichang 443004, China

Abstract: In this paper, 2-D computational analyses were conducted for unsteady high Reynolds number flows around a smooth circular cylinder in the supercritical and upper-transition flow regimes, i.e. $8.21 \times 10^4 < Re < 1.54 \times 10^6$. The calculations were performed by means of solving the 2-D Unsteady Reynolds-Averaged Navier-Stokes (URANS) equations with a $k-\epsilon$ turbulence model. The calculated results, produced flow structure drag and lift coefficients, as well as Strouhal numbers. The findings were in good agreement with previous published data, which also supplied us with a good understanding of the flow across cylinders of different high Reynolds numbers. Meanwhile, an effective measure was presented to control the lift force on a cylinder, which points the way to decrease the vortex induced vibration of marine structure in future.

Keywords: circular cylinder; vortex shedding; high Reynolds number; Strouhal numbers; lift control measure; marine structure; unsteady numerical simulation

Article ID: 1671-9433(2013)02-0180-05

1 Introduction

Recently, the unsteady viscous flow past bluff bodies and the resultant vortex shedding have been the focus of numerous numerical analyses and experimental investigations. This represents an idealized bluff body flow which has become of great interest for a wide range of engineering applications, such as hydrodynamic loading on marine pipelines, risers, offshore platform support legs, etc. Many of these engineering applications are often subject to flow conditions corresponding to high Reynolds number. Kawaguti and Jain (1966), Ingham (1968) conducted the first unsteady calculations of symmetric flow around a circular cylinder. Later, Keller and Takami (1966) first investigated the effect of domain size. Catalano *et al.* (2003) applied 3-D large eddy simulation with wall modeling as well as URANS using the standard $k-\epsilon$ model for $0.5 \times 10^6 < Re < 4 \times 10^6$. Singh and Mittal (2005) performed their studies for $100 < Re < 1 \times 10^7$. Franke *et al.* (1989) applied

URANS with the standard high Reynolds number $k-\epsilon$ model of Launder and Spalding (1972) at $Re = 1.4 \times 10^5$. Later, Tutar (2001) continued the investigation at the same Reynolds number using both the standard high Reynolds number $k-\epsilon$ model and non-linear $k-\epsilon$ model. Their results were mainly obtained for the flow in the subcritical flow regime at the start of the drag crisis. Thoman and Szweczyk (1969) computed transient solutions to a wide range of Re from 1 to 10^5 . In addition to drag, usually the pressure distribution, streamlines and vorticity contours were presented for several Reynolds numbers.

To date, a number of individual 2-D CFD simulations of cross sections along riser were combined with a full 3-D structural analysis to predict overall vortex-induced vibration (VIV) loads and displacement of the riser (2005). Thus, more computational and experimental research on high Reynolds number flows over a circular cylinder are necessary in order to have a better understating on hydrodynamic responses of marine structures.

In this paper, a variety Reynolds numbers at different flow velocity and diameter of cylinder were investigated by using the 2D Unsteady Reynolds-Averaged Navier-Stokes (URANS) equations with a $k-\epsilon$ turbulence model. The hydrodynamic force such as drag and lift along with the Strouhal number were discussed in great length. Meanwhile, pressure and vorticity distribution in the flow field were studied. The results appear to yield satisfactory agreements with the available data. At last, an effective measure was presented to decrease the lift force act on the cylinder in order to control the vortex induced vibration on marine structures.

2 Numerical method and solution procedure

Most real fluid-flow phenomena are mathematically represented by the well-known Navier-Stokes (N-S) equations, which are based on the continuum hypothesis. The N-S equations are a set of a nonlinear partial differential equations arrived at by conservation of transport properties such as mass, momentum and energy for an infinitesimal control volume. In vector notation they are as follows:

Conservation of mass,

Received date: 2012-12-04.

Revised date: 2013-01-04.

Foundation item: Supported by Supported by the National Natural Science Foundation of China (Grant No. 51009070).

***Corresponding author Email:** feng_dk@mail.hust.edu.cn

© Harbin Engineering University and Springer-Verlag Berlin Heidelberg 2013

$$\frac{\partial \rho}{\partial t} + \nabla \cdot (\rho \mathbf{u}) = 0 \quad (1)$$

Conservation of momentum,

$$\rho \frac{\partial \mathbf{u}}{\partial t} + \rho(\mathbf{u} \cdot \nabla) \mathbf{u} = -\nabla p + \nabla \cdot \boldsymbol{\tau} + \mathbf{f}_g \quad (2)$$

where

- $\nabla \cdot$ is the divergence operator;
- ∇ represents the gradient vector operator;
- ρ is the density of the fluid;
- p is thermodynamic pressure;
- \mathbf{u} stands for velocity vector;
- $\boldsymbol{\tau}$ is the stress tensor;
- \mathbf{f}_g stand for additional body forces.

The stress tensor $\boldsymbol{\tau}$ was expressed in terms of the velocity gradients by assuming the working fluid to be Newtonian which, using the Stoke's hypothesis is given by:

$$\boldsymbol{\tau} = \mu \text{def}(\mathbf{u}) - \frac{2}{3} \mu I (\nabla \cdot \mathbf{u}) \quad (3)$$

Here "I" denotes the unit tensor which is like the Kronecker delta in Cartesian tensor notation. Substituting the definition of the rate of deformation tensor $\text{def}(\mathbf{u})$ in the stress tensor and then taking the divergence of the conservation of momentum equation was reduced to what is normally called the Navier-Stokes equations:

$$\rho \frac{\partial \mathbf{u}}{\partial t} + \rho(\mathbf{u} \cdot \nabla) \mathbf{u} = -\nabla p + \nabla \cdot [\mu(\nabla \mathbf{u})] + \nabla \cdot [\mu(\nabla \mathbf{u})^T] + \mathbf{f}_g - \frac{2}{3} \nabla [\mu(\nabla \cdot \mathbf{u})] \quad (4)$$

The present study was not concerned with buoyancy effects, and so the body force due to gravity was assumed to be negligible, therefore defining pressure as:

$$P = p + \frac{2}{3} \mu(\nabla \cdot \mathbf{u}) \quad (5)$$

equation (2) can be reformulated in the following form:

$$\rho \frac{\partial \mathbf{u}}{\partial t} + \rho(\mathbf{u} \cdot \nabla) \mathbf{u} = -\nabla P + \nabla \cdot [\mu(\nabla \mathbf{u})] + \nabla \cdot [\mu(\nabla \mathbf{u})^T] \quad (6)$$

The basic assumptions used to derive the theoretical equations are summarized as follows:

The fluid was determined to be a continuum Newtonian Fluid;

- Stoke's hypothesis of incompressible fluid;
- No body forces or gravitational effect;
- Two dimensional geometry.

First, the simulation was able to solve the incompressible steady Reynolds Averaged Navier-Stokes (RANS) and continuity equations using the $k-\epsilon$ turbulent model. A second-order discretization method was used for the

convection. A second-order upwind scheme was also used for the viscous terms. When the steady solution achieved convergence, Unsteady Reynolds Averaged Navier-Stokes (URANS) was activated to continue calculation of the flow field around the cylinder. The results in this paper were obtained by the commercial code FLUENT.

3 Computational domain and boundary conditions

Fig.1 showed the size of computational domain. The computational domain was chosen for the circular cylinder as $45D$ in stream wise direction and $20D$ in the cross-stream wise direction. Here D was the cylinder diameter. This domain was chosen large enough to enable obtaining oscillation of the wake down-stream of the cylinder. The inlet of the domain was located on the left hand side of the cylinder at a distance of $15D$ from the center of the cylinder and the outlet of the domain was located at $30D$ from the center of the cylinder on the down-stream side, i.e. on the right hand side of the domain. The cross-stream boundaries were located $15D$ away from the center of the cylinder in upward and downward directions respectively. Computations were carried out for water as the fluid.

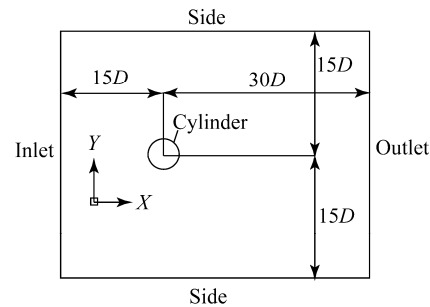


Fig. 1 Sketche of computational domain

The boundary conditions used for the numerical simulations are as follows:

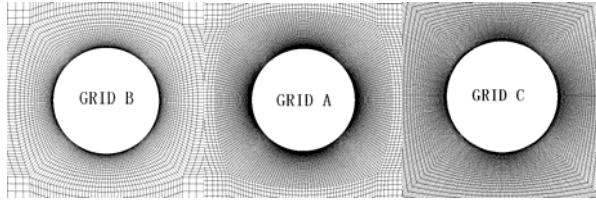
- 1) Inlet: velocity inlet. Uniform flow was specified at the inlet with $u_1=U_0$, $U_2=0$. The free stream inlet turbulence values of kinetic energy ($k = 3.75v^2/1000$) and turbulent dissipation ($\epsilon = k^{3/2}/0.03$) were given by Tutar (2001).
- 2) Outlet: pressure outlet. The flow was supposed to be fully developed when reaching outlet boundary.
- 3) Cylinder: wall. No-slip wall condition was applied on the rigid cylinder surface with $u_1=u_2=0$.
- 4) Side: velocity. The region was far from the circular cylinder enough that the flow was specified to be the same as uniform flow with $u_1=U_0$, $U_2=0$.

4 Grid independence and grid structure

Three cases with different total grids were first simulated to achieve a fine resolution of the region in this research. The diameter of the cylinder was 80mm, and the velocity

was 20 kn (10.288 m/s). Here the Reynolds number was 8.21×10^5 . The grids number was 34,300 (GRID B), 68,600 (GRID A) and 137,200 (GRID C).

The region close to the circular cylinder of the three grids was shown in Fig. 2. Drag coefficient (C_d) of the rigid cylinder obtained by different grids are shown in Table 1.



Left: GRID B (34,300); Middle: GRID A (68,600);
Right: GRID C (137,200)

Fig.2 Zoom of the grid in the vicinity of the cylinder

Table 1 C_d comparison of different grid

GRID model	GRID A	GRID B	GRID C
Elements	68 600	34 300	137 200
C_d	0.5058	0.5051	0.5059

There was good consistence between the results of C_d obtained by different grid, which indicates that the simulation in this research has good grid independence. Thus, the latter investigation was based on Grid B which makes the simulation more efficient. Fig. 3 shows mesh in the computational domain.

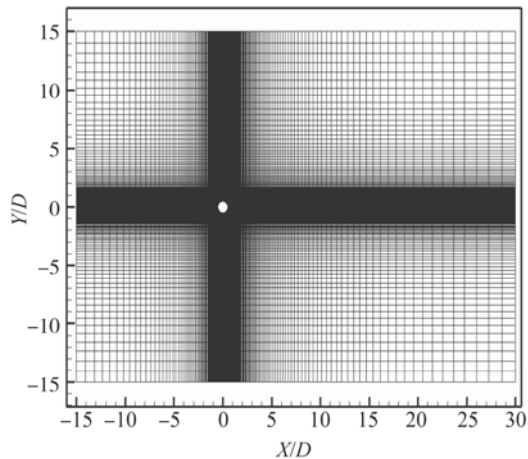


Fig.3 The computational mesh of the domain

5 Results and discussion

The velocity in this paper ranges from 8kn (4.12m/s) to 30kn (15.43m/s), and the diameter ranges from 20mm to 100mm. Thus, the Reynolds number was between 8.21×10^4 and 1.54×10^6 . A steady time step ($\Delta t = 10^{-04}$ s) was used in the simulation. The time step was small enough to capture the vortex-shedding motion with a periodic vortex street qualitatively. Fig. 4 shows an example of contours of velocity magnitude for the rigid cylinder ($D=80$ mm) in

varying incoming flow. It appears that the present model was able to produce the periodic Karman vortex street efficiently. Fig. 5 shows the periodic fluctuation of lift forces along with the flow time. The rigid cylinder ($D=80$ mm) in each incoming velocity has a steady motion of vortex shedding. It appears that the period of lift force and the peak of lift coefficient is related to the velocity. The high speed case seems have a low vortex shedding period and small lift coefficient peak in Fig.5.

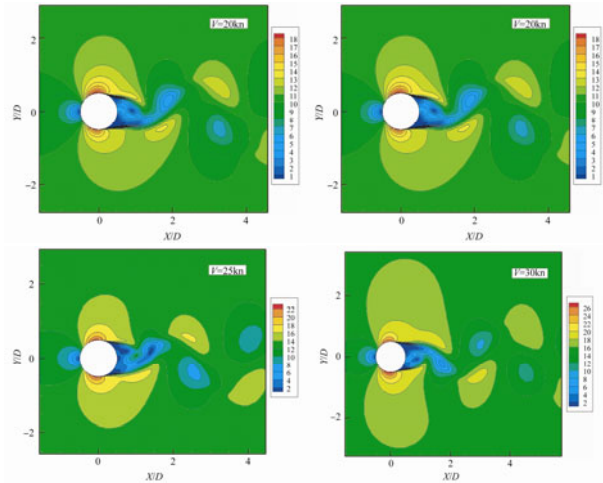


Fig.4 Instantaneous velocity magnitude contours of flow across a rigid cylinder at variety incoming velocity

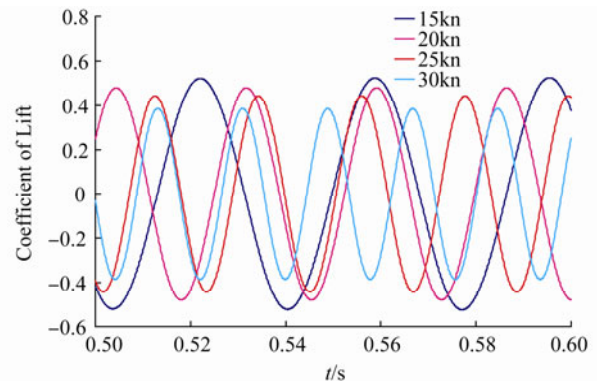


Fig.5 Lift coefficient of various velocity ($D=80$ mm)

Fig.6 shows the simulated mean pressure distribution ($C_p = (p_c - p_\infty) / (0.5 \rho U_\infty^2)$) at $Re = 1.03 \times 10^6$ ($V=25$ kn, $D=80$ mm) compared with the simulation results by Ong (2009) at $Re = 1.0 \times 10^6$. Here p_c is the static pressure on the surface of the circular cylinder, θ measured clockwise from the stagnation point; and p_∞ is the static pressure of the flow at infinity. The present simulation results have a good agreement with the results reported by Ong (2009). The discrepancy between the present results and the simulation results by Muk Chen Ong might be due to the different implementations of the wall function. Of course,

there was a small difference in the Reynolds number which creates a little inconformity in the results.

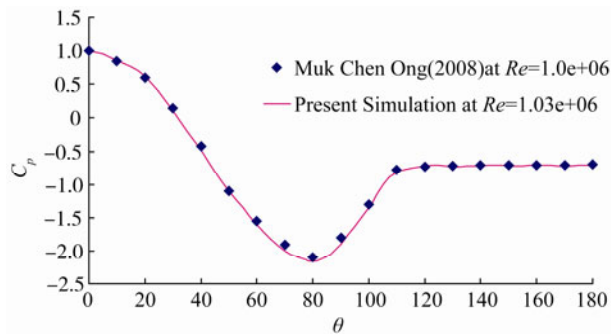


Fig. 6 Mean pressure distribution on the cylinder at $Re=1.03 \times 10^6$

Fig.7 shows the drag coefficient in the different cases simulated in this paper. It was illustrated that the drag coefficient was inverted to the incoming velocity. The drag coefficient had the same tendency along with the diameter of the circular cylinder at the different velocity. The results indicate the circular cylinder velocity goes up in some range and then apparently comes back down. It would be reasonable to believe that it is the drag crisis (sudden loss of drag at $Re=2 \times 10^5$) that should take responsibility for the phenomenon.

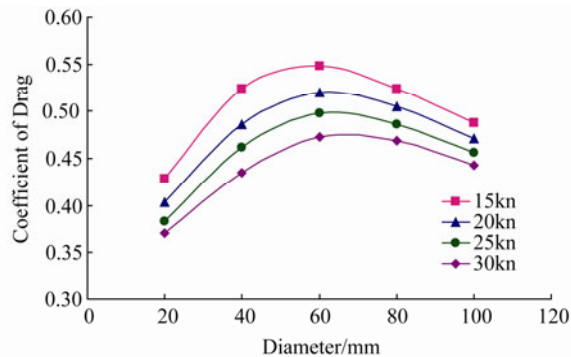


Fig.7 Drag coefficient of various cases

Strouhal number is proportional to the reciprocal of vortex spacing expressed as number of obstacle diameters and is used in momentum transfer in general von Karman vortex streets and unsteady state flow calculations in particular. It is normally defined in the following form:

$$St = \frac{fD}{U} \quad (7)$$

where f is the frequency of vortex shedding, D is the diameter of the circular cylinder and U is the incoming velocity. In the present study the Strouhal number is calculated based on the periodic fluctuation of lift forces, as they are consequence of the vortex shedding. The time period for one cycle is calculated from the graph of coefficient of Lift plotted against the time. Fig.8 shows the Strouhal number of different cases investigated in the research. The Strouhal number ranges

from 0.28 to 0.31 in the Reynolds number simulation in this paper. The results are in accordance with the published data Lienhard (1966).

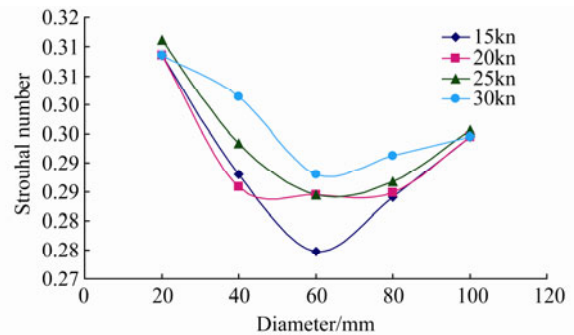
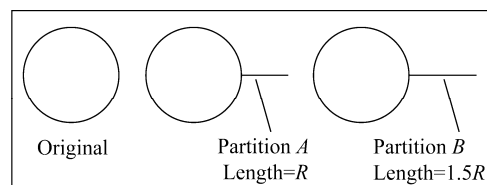


Fig. 8 Strouhal number of various cases

6 Lift force control measure

The 2-D CFD simulation results of cross sections along riser combined with a full 3-D structural analysis were able to predict overall vortex-induced vibration (VIV) loads and displacement of the riser. Thus, it can be guessed that decreasing the lift force on the cross section along riser is an effective measure to control the vortex-induced vibration. A partition is set rear the cylinder on the center line of the flow field. Fig.9 is the sketch of the partition. The length of the partition is equal to the radius of the circular cylinder in partition A and $1.5R$ in partition B.



Left: Original cylinder; Middle: Partition A (Length=R); Right: Partition B (Length=1.5R)

Fig. 9 Sketch of the partition

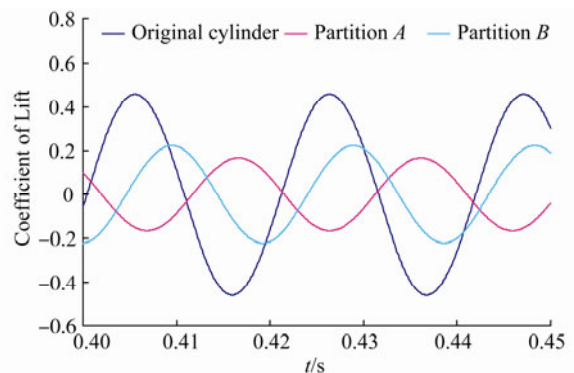


Fig. 10 Lift coefficient of three cases

Fig.10 shows the lift coefficient along with the time of the three cases simulated in this part. In the case of original cylinder, the lift force is generated from the surface of the rigid cylinder. Nevertheless, the lift force comes from the

surface of the circular cylinder and the partition in the case of partition *A* and partition *B*. It could be easily found that the cases with a partition have an obvious decrease of the lift force. The peak comes down nearly a half. The length of partition also has a significant influence on the lift force of the circular cylinder. The partition *A* case has had a better performance in lift force control than partition *B*. The lift force of partition *A* has had a decrease of 30% compared to partition *B* case. It can be assumed that the lift force was controlled by the valid measure.

Fig. 11 is the velocity field rear to the original cylinder and partition *A*. It shows that the low speed region was stretched in the case of partition *A*. The place of vortex shedding was retarded and closer to the center line of the wake. Meanwhile, the velocity distribution rear the cylinder has a better symmetrical characteristic than the original cylinder to some extent. Thus, it would be reasonable to believe that the partition changing the velocity distribution of the region behind the circular cylinder contributes to the decrease of lift force.

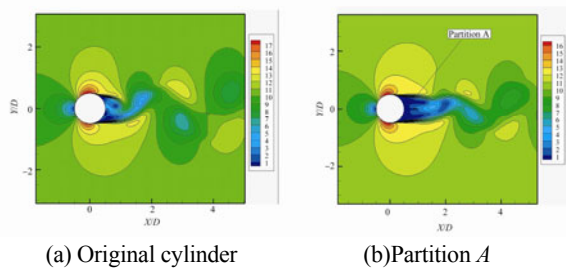


Fig.11 Velocity distribution in the rear the rigid cylinder

7 Conclusions

A detailed numerical investigation for two-dimensional circular cylinder at various high Reynolds number was carried out in the present study. An efficient finite volume code employing a multi-grid refinement technique leads to good results for drag coefficient, and Strouhal number. The simulation captures the Karman vortex street phenomenon. Meanwhile, the results of present study have a fine agreement with available published literature.

A special measure was proposed to control the lift force of cylinder. The partition changes the distribution of velocity and makes the peak of lift force decrease more than half. It was an efficient measure to control the vortex-induced vibration for some marine structure. Further attention should be paid on the 3-D numerical study of cylinder at high Reynolds numbers.

References

Caralano P, Wang M, Iaccarino G, Moin P (2003). Numerical

simulation of the flow around a circular cylinder at high Reynolds numbers. *Int. J. Heat Fluid Flow*, **24**, 463-469.

Chaplin JR, Bearman PW, Cheng Y, Fontaine E, Graham JMR, Herfjord K (2005). Blind predictions of laboratory measurements of vortex-induced vibrations of a tension riser. *J. Fluids Structures*, **21**, 25-40.

Franke R, Rodi W (1989). Analysis of experiment vortex shedding data with respect to turbulence modeling. *Proceedings of the 7th Turbulent Shear Flow Symposium*, Stanford, USA, 24.4.4-24.4.5.

Ingham DB (1968). Note on the numerical solution for unsteady viscous flow past cylinder. *J. Fluid Mech.*, **31**(4), 815-818.

Kawaguti M, Jain P (1966). Numerical study of a viscous flow past a circular cylinder. *J. Phys. Soc. Japan*, **21**(10), 2055-2062.

Keller HB, Takami H (1966). *Numerical studies of steady viscous flow about cylinders*. In: Greenspan D, editor. *Numerical Solutions of Nonlinear Differential Equations*. Wiley, New York, 115-140.

Lauder BE, Spalding DB (1972). *Mathematical models of turbulence*. Academic Press, London.

Lienhard JH (1966). Synopsis of lift, drag and vortex frequency data for rigid circular cylinders. *Washington State University, College of Engineering, Research Division Bulletin 300*.

Ong MC, Utne T, Holmedal LE, Myrhaug D, Pettersen B (2009). Numerical simulation of flow around a smooth circular cylinder at very high Reynolds numbers. *Marine Structures*, **22**(2), 142-153.

Singh SP, Mittal S (2005). Flow past a cylinder: shear layer instability and drag crisis. *Int. J. Numer. Meth. Fluids*, **47**, 75-98.

Thoman DC, Szewczyk AA (1969). Time dependent viscous flow over circular cylinder. *Phys. Fluids Suppl. II*, **12**, 76-86.

Tutar M, Hold AE (2001). Computational modeling of flow around a circular cylinder in sub-critical flow regime with various turbulence models. *Int. J. Numer. Meth. Fluids*, **35**, 763-84.

Author biographies



Yanhui Ai is senior engineer. He graduated from the Harbin Engineering University, Haibin, China, in 2002 with a master degree in ship engineering. He continued post graduate studies in the field of hydrodynamic at HuaZhong University of Science and Technology (HUST), WuHan, China, and graduated in 2013 with a doctor degree. Now, he is engaged in hydromechanics and design of underwater towing system.



Dakui Feng is instructor. He graduated from HuaZhong University of Science and Technology (HUST), WuHan, China, in 2008 with a doctor degree in ship engineering. Now, he is engaged in hydromechanics and research of navigation body's fluid dynamic character.